

---

# Unsupervised discovery of the shared and private geometry in multi-view data

---

**Sai Koukuntla**

Department of Biomedical Engineering  
Johns Hopkins University  
Baltimore, MD 21218  
skoukun1@jh.edu

**Joshua B. Julian**

Princeton Neuroscience Institute  
Princeton University  
Princeton, NJ 08540  
jjulian@princeton.edu

**Jesse C. Kaminsky**

Princeton Neuroscience Institute  
Princeton University  
Princeton, NJ 08540  
jk8386@princeton.edu

**Manuel Schottdorf**

Princeton Neuroscience Institute  
Princeton University  
Princeton, NJ 08540  
ms81@princeton.edu

**David W. Tank**

Princeton Neuroscience Institute  
Princeton University  
Princeton, NJ 08540  
dwtank@princeton.edu

**Carlos D. Brody<sup>†</sup>**

Princeton Neuroscience Institute  
Princeton University  
Princeton, NJ 08540  
brody@princeton.edu

**Adam S. Charles<sup>†</sup>**

Department of Biomedical Engineering  
Center for Imaging Science  
Kavli Neurodiscovery Institute  
Johns Hopkins University  
Baltimore, MD 21218  
adamsc@jhu.edu

## Abstract

Modern applications often leverage multiple views of a subject of study. Within neuroscience, there is growing interest in large-scale simultaneous recordings across multiple brain regions. Understanding the relationship between views (e.g., the neural activity in each region recorded) can reveal fundamental principles about the characteristics of each representation and about the system. However, existing methods to characterize such relationships either lack the expressivity required to capture complex nonlinearities, describe only sources of variance that are shared between views, or discard geometric information that is crucial to interpreting the data. Here, we develop a nonlinear neural network-based method that, given paired samples of high-dimensional views, disentangles low-dimensional shared and private latent variables underlying these views while preserving intrinsic data geometry. Across multiple simulated and real datasets, we demonstrate that our method outperforms competing methods. Using simulated populations of lateral geniculate nucleus (LGN) and V1 neurons we demonstrate our model's ability to discover interpretable shared and private structure across different noise conditions.

---

<sup>†</sup> Please direct correspondence to CDB (brody@princeton.edu) and ASC (adamsc@jhu.edu).

On a dataset of unrotated and corresponding but randomly rotated MNIST digits, we recover private latents for the rotated view that encode rotation angle regardless of digit class, and places the angle representation on a 1-d manifold, while shared latents encode digit class but not rotation angle. Our approach, when compared to the current state of the art, results in a quantifiably significantly better isolation between the shared and private information. Applying our method to simultaneous Neuropixels recordings of hippocampus and prefrontal cortex while mice run on a linear track, we discover a low-dimensional shared latent space that encodes the animal’s position. We propose our approach as a general-purpose method for finding succinct and interpretable descriptions of paired data sets in terms of disentangled shared and private latent variables.

## 1 Introduction

Many modern applications require the ability to identify and interpret the relationships between multiple high-dimensional datasets that represent multiple views of the same underlying system. Examples exist across applications, for example the shared semantic overlap between text captions and images; finding the underlying variables shared between counts of mRNA transcripts and protein counts [2]; and performing sensor fusion in robotics [10]. This paradigm of multi-view data is becoming increasingly important in neuroscience with the rapid growth of new recording technologies that enable recording of many neurons in multiple brain regions simultaneously [22, 41, 4]. Each brain region can be thought of as a view into the underlying brain-wide activity. We then wish to understand what information is encoded in each brain area separately and which information is shared in a joint computation. Operating on the individual brain areas’ activity is confounded by the joint, nonlinear mixing of these two information types; shared and private.

To enable a deeper understanding and interpret which computations are local and which are global, we thus need to *disentangle* these different information types. However, disentangling by itself is insufficient for understanding; assessing the intrinsic geometry of the disentangled shared and private data can provide fundamental clues towards extracting biological insight into how the brain structures internal representations of information within and across regions. For example, work from single regions has demonstrated a ring geometry in the population activity of head direction cells, enabling blind discovery and decoding of the represented variable [5], predictions of theoretical continuous attractor models of the entorhinal cortex grid cell system have been confirmed through topological analysis of experimental data that indicated a toroidal geometry in the activity of that population of neurons [13], and geometry-preserving retinotopic maps have been used to delineate the borders of different but adjacent visual regions [9, 56]. However, extending geometry-estimation approaches to multiple regions is complicated by the fact that brain regions typically multiplex several different types of information. Estimating the geometry of the information specifically shared with another region therefore requires being able to separate the private from the shared information.

In general, characterizing the geometry of data has been the domain of dimensionality reduction [7, 46, 33], and more specifically manifold learning [45, 40, 37]. These methods primarily focus on quantifying the latent relationships between data points through either learning graphs on data [26, 34, 15, 26, 28] or by estimating geodesic paths that define the manifold surface, e.g., [44, 6, 35]. These approaches effectively treat a local distance between nearby data points as a first step or as a primary quantity that is to be retained in the learned structure. Shared data manifolds in multi-view data typically extend these ideas as a “union” operator, i.e., data from both views are merged into a single manifold where local distances in each dataset form the basis for the embedding [11, 55, 36]. Unfortunately, when there is a mix of private and shared information in each view, the private information can cause significant deviations in the computed local distances, skewing any hope of embedding points with similar shared information but different private information together. This effect becomes more pronounced as the amount of private and shared information become comparable. Therefore a critical step in learning the geometry of each of the shared and private sub-manifolds is to first disentangle the shared and private information.

Thus, a key requirement of this endeavor are methods that can extract from two distinct but paired datasets ( $\mathbf{A}$  and  $\mathbf{B}$ ) a single model that captures the maximal variance jointly in both datasets and separates the shared and private representations. Mathematically, we can phrase this task as an inverse problem where, for any sample of paired data points  $\mathbf{x}_A \in \mathbf{A}$  and  $\mathbf{x}_B \in \mathbf{B}$ , there exist a

shared set of variables  $\mathbf{s}$  and two private sets of variables  $\mathbf{z}_A$  and  $\mathbf{z}_B$  such that  $\mathbf{x}_A = g_A(\mathbf{s}, \mathbf{z}_A)$  and  $\mathbf{x}_B = g_B(\mathbf{s}, \mathbf{z}_B)$  for two distinct nonlinear functions  $g_A(\cdot)$  and  $g_B(\cdot)$ , where  $\mathbf{z}_A$ ,  $\mathbf{s}$  and  $\mathbf{z}_B$  are all statistically independent (i.e., "disentangled"). Our goal is to find  $\{g_A(\cdot); g_B(\cdot); \mathbf{z}_A; \mathbf{s}; \mathbf{z}_B\}$ .

This formulation is very general, in the sense that any joint distribution  $p(\mathbf{A}, \mathbf{B})$  can be described this way. But it is also not unique: many possible forms of  $\{g_A(\cdot); g_B(\cdot)\}$  and corresponding representations  $\{\mathbf{z}_A, \mathbf{s}, \mathbf{z}_B\}$  can be used to describe a given joint distribution  $p(\mathbf{A}, \mathbf{B})$ . Some of these representations will be more easily interpreted than others. Here we follow [43] in positing that representations that preserve intrinsic data geometry are likely to be more interpretable than those that don't. Unfortunately, estimating shared or private geometry in the data space is extremely difficult as any measures of distance can be skewed by the potentially nonlinear mixing between their latents. Thus estimating geometry is much more natural in the disentangled representation  $\{\mathbf{z}'_A, \mathbf{s}', \mathbf{z}'_B\}$ . Specifically, we can seek a bijective transformation of each of these latent spaces to obtain a final representation  $\{\mathbf{z}_A, \mathbf{s}, \mathbf{z}_B\}$  that preserves each of their intrinsic data geometries.

Due to the importance of this task across fields, many methods have been developed to try and address the disentangling of private and shared latents. These methods either suffer from limitations in expressibility, e.g., by modeling the latent spaces as linear [21, 30, 42], limitations in generalization by only embedding the current dataset non-parametrically [28], imperfect separation of private and shared information, e.g., via not modeling the private latents [27, 1, 48, 53, 23, 49], or failing to preserve intrinsic geometry [31, 52]. There thus exists a need for a robust model that can disentangle highly nonlinearly mixed shared and private information from multi-view data while preserving the data geometry.

In this work we therefore present a new model—Submanifold Partitioning via Least-variance Informed Channel Estimation (SPLICE)—that extracts the shared and private geometries, i.e., their respective submanifolds from a multi-view dataset. Our approach is based on an autoencoder with a "cross butterfly" architecture that splits the latent state into shared and private variables. Our framework simultaneously minimizes the error in recovering the data from the shared and private variables together, while minimizing the ability of each dataset's private latent space to predict the other's. Given this disentangled representation, our approach then projects data points onto the shared and private submanifolds and leverages a cost function based geodesic distance preservation [40] that retains the structure of the private and the shared latent spaces.

The primary contributions of our work are: 1) a new network architecture (SPLICE) that separates and captures both the shared and private intrinsic geometry of two datasets, 2) validation of the architecture in controlled simulations of LGN-V1 connections 3) multiple real-data examples showing that our network can correctly separate highly nonlinear relationships in very few latent variables, and 4) comparison to the state-of-the-art methods [31, 49, 23], demonstrating superior disentangling and geometry preservation in highly nonlinear mixing conditions.

## 2 Related Work

### 2.1 Related work in neuroscience

Within neuroscience, significant progress in assessing the relationship between activity in different brain regions has already been achieved using models that assume either a linear link between latent variables and neural activity [39, 18, 17, 8, 12], or linear followed by a pointwise nonlinear function such as  $\text{softplus}(\cdot)$  or exponential [16, 3, 24]. In terms of artificial neural networks, all of these can be thought of as having a single, potentially nonlinear, layer between latent variables and predicted neural activity. The advances in many of these studies are related to the temporal dynamics of the latent variables, an aspect not addressed here. Some of the studies explicitly distinguish latents labeled as shared versus latents labeled as private to each region. However, an important issue is that many, perhaps most, neural representations are known to be nonlinear. As a single example that we will return to below, the activity of visual neurons in the lateral geniculate nucleus (LGN) or primary visual cortex (V1) in response to a bar of light is not a linear (or monotonic, like  $\text{softplus}(\cdot)$  or exponential) function of bar position. This suggests that many datasets may not be well described with linear or generalized linear approaches. Here we allow more complex nonlinear relationships by using link functions parametrized by deep neural networks.

## 2.2 Related work in machine learning

### 2.2.1 Identification and separation of private and shared latent variables

In classical statistics, canonical correlation analysis [20] is an important linear method to obtain a shared description of two views  $\mathbf{x}_A$  and  $\mathbf{x}_B$ . Using a notation where  $A \rightarrow A$  will mean "from view  $A$  to shared description  $A$ ", the essential idea is to find the two matrices  $\mathbf{F}_{A \rightarrow A}$  and  $\mathbf{F}_{B \rightarrow B}$  such that  $\mathbf{F}_{A \rightarrow A} \cdot \mathbf{x}_A$  and  $\mathbf{F}_{B \rightarrow B} \cdot \mathbf{x}_B$  will be maximally correlated with each other:

$$\begin{aligned} \mathbf{F}_{A \rightarrow A}^*, \mathbf{F}_{B \rightarrow B}^* &= \arg \min_{\mathbf{F}_{A \rightarrow A}, \mathbf{F}_{B \rightarrow B}} -\text{Tr} \left( \mathbb{E} \left[ (\mathbf{F}_{A \rightarrow A} \cdot \mathbf{x}_A) (\mathbf{F}_{B \rightarrow B} \cdot \mathbf{x}_B)^T \right] \right) \\ \text{subject to} \quad &\mathbb{E} \left[ (\mathbf{F}_{i \rightarrow i} \cdot \mathbf{x}_i) (\mathbf{F}_{i \rightarrow i} \cdot \mathbf{x}_i)^T \right] = \mathbf{I} \quad \text{for } i = A, B \end{aligned} \quad (1)$$

Deep canonical correlation analysis (DCCA) [1] extends this to the nonlinear setting by replacing the linear matrices with deep feedforward neural networks with parameters  $\theta_{F_A}^s$  and  $\theta_{F_B}^s$ , namely  $F_{A \rightarrow A}(\cdot; \theta_{F_A}^s)$  and  $F_{B \rightarrow B}(\cdot; \theta_{F_B}^s)$ . We will refer to these networks as "encoder" networks, and their outputs as "putatively shared latents":

$$\underbrace{\widehat{\mathbf{s}}_A}_{\text{shared A latent}} = F_{A \rightarrow A}(\mathbf{x}_A; \theta_{F_A}^s), \quad \underbrace{\widehat{\mathbf{s}}_B}_{\text{shared B latent}} = F_{B \rightarrow B}(\mathbf{x}_B; \theta_{F_B}^s) \quad (2)$$

$$\begin{aligned} \theta_{F_A}^{s*}, \theta_{F_B}^{s*} &= \arg \min_{\theta_{F_A}^s, \theta_{F_B}^s} -\text{Tr} \left( \mathbb{E} \left[ \widehat{\mathbf{s}}_A \cdot \widehat{\mathbf{s}}_B^T \right] \right) \\ \text{subject to} \quad &\mathbb{E} \left[ \widehat{\mathbf{s}}_i \cdot \widehat{\mathbf{s}}_i^T \right] = \mathbf{I} \quad \text{for } i = A, B \end{aligned} \quad (3)$$

While this approach is powerful for finding nonlinear transforms that extract information shared between the two views, it has no mechanism to encourage that *all*, or even most, of the shared information would be identified and be present in the shared latents  $\mathbf{s}_A$  and  $\mathbf{s}_B$ . To address this issue, [50] introduces Deep Canonical Correlation Autoencoders (DCCA), in which decoder networks  $G_A(\cdot; \theta_{G_A})$  and  $G_B(\cdot; \theta_{G_B})$  operate on  $\mathbf{s}_A$  and  $\mathbf{s}_B$ , and attempt to reconstruct the two original views  $\mathbf{x}_A$  and  $\mathbf{x}_B$ :

$$\begin{aligned} \underbrace{\widehat{\mathbf{x}}_A^{\text{pred}}}_{\text{A reconstruction}} &= G_A(\widehat{\mathbf{s}}_A; \theta_{G_A}), \quad \underbrace{\widehat{\mathbf{s}}_A}_{\text{shared A latent}} = F_{A \rightarrow A}(\mathbf{x}_A; \theta_{F_A}^s), \\ \underbrace{\widehat{\mathbf{x}}_B^{\text{pred}}}_{\text{B reconstruction}} &= G_B(\widehat{\mathbf{s}}_B; \theta_{G_B}), \quad \underbrace{\widehat{\mathbf{s}}_B}_{\text{shared B latent}} = F_{B \rightarrow B}(\mathbf{x}_B; \theta_{F_B}^s) \\ \theta &= [\theta_{G_A}, \theta_{G_B}, \theta_{F_A}^s, \theta_{F_B}^s] \\ \theta^* &= \arg \min_{\theta} \left\{ \underbrace{\beta_1 \left| \widehat{\mathbf{x}}_A^{\text{pred}} - \widehat{\mathbf{x}}_A \right|^2 + \beta_1 \left| \widehat{\mathbf{x}}_B^{\text{pred}} - \widehat{\mathbf{x}}_B \right|^2}_{\text{reconstruction loss}} - \underbrace{\text{Tr} \left( \mathbb{E} \left[ \widehat{\mathbf{s}}_A \cdot \widehat{\mathbf{s}}_B^T \right] \right)}_{\text{DCCA loss}} \right\} \\ \text{subject to} \quad &\mathbb{E} \left[ \widehat{\mathbf{s}}_i \cdot \widehat{\mathbf{s}}_i^T \right] = \mathbf{I} \quad \text{for } i = A, B \end{aligned} \quad (4)$$

Minimizing the reconstruction loss to zero would imply that  $G_A(\mathbf{s}_A)$  and  $G_B(\mathbf{s}_B)$  reconstructed the inputs  $\mathbf{x}_A$  and  $\mathbf{x}_B$  perfectly, and would therefore guarantee that no information about  $\mathbf{x}_A$  and  $\mathbf{x}_B$  was absent from  $\mathbf{s}_A$  and  $\mathbf{s}_B$ .

However, one view may contain information that is specific to it and not shared with the other (the private information). Attempting to preserve *all* information in  $\mathbf{s}_A$  and  $\mathbf{s}_B$  (e.g. through perfect reconstruction) implies including some private information. We refer to this as private information leaking into the putatively shared information latents. That leakage will hinder the DCCA loss, for private information cannot be matched across the two views. Thus the reconstruction loss terms and the DCCA loss terms need to trade off with each other: it is impossible to optimize both simultaneously. Addressing this in an autoencoder framework requires having not only latent variables  $\mathbf{s}_A$  and  $\mathbf{s}_B$  for the shared information, but also putatively private latent variables  $\mathbf{z}_A$  and  $\mathbf{z}_B$ , obtained through their own encoders ( $\mathbf{z}_A = F_A(\mathbf{x}_A)$  and  $\mathbf{z}_B = F_B(\mathbf{x}_A)$ ) that capture the private information specific to each view. [51] introduces such an approach, and also places the problem within a variational framework, in which the prior distribution of the latents is an isotropic Gaussian. This factorized prior is used to encourage mutual independence between the inferred private and shared latents. DMVAE [29] also uses a variational approach, but more strongly encourages disentangling through by minimizing the "total correlation": the KL divergence between the joint latent distribution and the product of the marginal latent distributions.

While the isotropic Gaussian prior and total correlation approaches of [51] encourage independence of the private and shared latents, they do not guarantee it. [31] recognized that proposes using the DCCA framework of [50] with the addition of private latents, but adds inner DCCA networks that seek information in common between the shared and private latents  $\mathbf{s}_A$  and  $\mathbf{z}_A$ . They reason that if  $\mathbf{s}_A$  and  $\mathbf{z}_A$  were not independent, the inner DCCA network would find some correlated view of them. On this basis, they propose an adversarial training scheme in which (a) the inner DCCA network trains to maximize its identification of a relationship between  $\mathbf{s}_A$  and  $\mathbf{z}_A$ ; while (b) the encoder networks  $F_{A \rightarrow A}(\cdot)$  and  $F_A(\cdot)$  train to produce inputs  $\mathbf{s}_A$  and  $\mathbf{z}_A$  to that inner DCCA network that minimize the correlation that the inner DCCA network can find. This adversarial scheme thus seeks an outcome where the DCCA network is well trained, but it can find no information in common between  $\mathbf{s}_A$  and  $\mathbf{z}_A$ , in which case  $\mathbf{s}_A$  and  $\mathbf{z}_A$  must be independent. This is the desired disentanglement. The same procedure is followed with  $\mathbf{s}_B$  and  $\mathbf{z}_B$ . (Below, we will adopt a closely related adversarial approach.) Simultaneously with (b), and following the DCCA approach, the encoder and decoder networks  $F_{A \rightarrow A}(\cdot)$ ,  $F_A(\cdot)$ ,  $G_A(\cdot)$ ,  $F_{B \rightarrow B}(\cdot)$ ,  $F_B(\cdot)$ ,  $G_B(\cdot)$  are trained to minimize the the DCCA loss.

[31] thus propose:

$$\begin{aligned}
 \underbrace{\widehat{\mathbf{x}}_A^{pred}}_{\text{A reconstruction}} &= G_A(\widehat{\mathbf{s}}_A, \widehat{\mathbf{z}}_A; \theta_{G_A}), & \underbrace{\widehat{\mathbf{s}}_A}_{\text{shared A latent}} &= F_{A \rightarrow A}(\mathbf{x}_A; \theta_{F_A}^s), & \underbrace{\widehat{\mathbf{z}}_A}_{\text{private A latent}} &= F_A(\mathbf{x}_A; \theta_{F_A}), \\
 \underbrace{\widehat{\mathbf{x}}_B^{pred}}_{\text{B reconstruction}} &= G_B(\widehat{\mathbf{s}}_B, \widehat{\mathbf{z}}_B; \theta_{G_B}), & \underbrace{\widehat{\mathbf{s}}_B}_{\text{shared B latent}} &= F_{B \rightarrow B}(\mathbf{x}_B; \theta_{F_B}^s), & \underbrace{\widehat{\mathbf{z}}_B}_{\text{private B latent}} &= F_B(\mathbf{x}_B; \theta_{F_B}) \\
 \theta &= [\theta_{G_A}, \theta_{G_B}, \theta_{F_A}^s, \theta_{F_B}^s, \theta_{F_A}, \theta_{F_B}] \\
 \mathcal{L}_{DCCA E} &= \underbrace{\beta_1 \left| \widehat{\mathbf{x}}_A^{pred} - \widehat{\mathbf{x}}_A \right|^2 + \beta_1 \left| \widehat{\mathbf{x}}_B^{pred} - \widehat{\mathbf{x}}_B \right|^2}_{\text{reconstruction loss}} - \underbrace{\text{Tr} \left( \mathbb{E} \left[ \widehat{\mathbf{s}}_A \cdot \widehat{\mathbf{s}}_B^T \right] \right)}_{\text{DCCA loss}}
 \end{aligned}$$

Inner DCCA networks between private and shared latents: For  $i = A, B$  :

$$\widehat{\mathbf{v}}_i^1 = H_i^1(\widehat{\mathbf{s}}_i; \theta_{H_i^1}), \quad \widehat{\mathbf{v}}_i^2 = H_i^2(\widehat{\mathbf{z}}_i; \theta_{H_i^2}),$$

$$\theta_i = \left[ \theta_{H_i^1}, \theta_{H_i^2} \right]$$

$$\mathcal{L}_{\text{inner DCCA } i} = -\text{Tr} \left( \mathbb{E} \left[ \widehat{\mathbf{v}}_i^1 \cdot \widehat{\mathbf{v}}_i^{2T} \right] \right)$$

$$\theta^* = \arg \min_{\theta_{F_a}, \theta_{F_b}} \left\{ \sup_{\theta_{H_i^1}, \theta_{H_i^2}} \mathcal{L}_{\text{inner DCCA } i} \right\}$$

subject to  $\mathbb{E} \left[ \hat{\mathbf{v}}_i^j \cdot \hat{\mathbf{v}}_i^{jT} \right] = \mathbf{I}$  for  $j = 1, 2$  and  $i = A, B$

and  $\mathbb{E} \left[ \hat{\mathbf{s}}_i \cdot \hat{\mathbf{s}}_i^T \right] = \mathbf{I}$  for  $i = A, B$  (5)

[47] also addressed this problem, but only within the strong constraint of a generative model in which the generating functions  $g_A()$  and  $g_B()$  are identical to each other. This constraint will in general not be satisfied when the two views are the activity of two different brain regions, and we do not consider it further here. [54] focused on proofs of identifiability of the latent variables, and for private versus shared latent identification and separation, referred to the methods of [31].

To our knowledge, [31] represents the current state of the art in identification and separation of both private and shared latent variables. Nevertheless, the approach in [31] contains two problems that can prevent separation of the true private and shared information. The first problem is that guaranteeing that the *inferred* private and shared latents are mutually independent (as achieved by the adversarial training with the inner DCA network) does not also guarantee that the *true* private and shared information has been cleanly allocated to the inferred private and shared latents, respectively. For example, if the true private information is composed of multiple, mutually independent components, one of these true private components could be (incorrectly) present in the inferred putatively shared latent, and (incorrectly) absent from the inferred putatively private latent, yet because the *inferred* private and shared latents would be mutually independent, the inner DCCA network would have no way of detecting and correcting the problem. As with the DCCAE above, the presence of private information in a putatively shared latent would hinder the DCCA loss, but would help the reconstruction loss, and tradeoff between those two loss terms would prevent removal of the true private information from the putatively shared latents.

[23] introduces an approach that helps to correct the issue. We refer to this approach as a "crossed" autoencoder, and below we will adopt it here: the shared latent used to reconstruct one view is always computed from the other view. Thus it cannot possibly contain information private to the view it is being used to reconstruct. The crossed encoder approach therefore guarantees that no private information leaks into the shared latents. While [23] argues that downstream tasks do not require estimation of private latents and advocates focusing on estimating shared latents only, we have a main interest in understanding the neural representations of activity in the two views, not on downstream tasks. Consequently, while for completeness we will compare our results to those of [23], we will pursue estimation of the private latents as well as the shared ones. To do this, we also require a way to prevent the opposite leakage scenario, leakage into the private latents of a component of the true shared information, whether or not that shared information is present in the inferred shared latents. None of the CCA correlation terms, the reconstruction loss term, or the inner DCCA adversarial training would be able to disentangle the private latents shared information that is not present in the shared latents. To solve this final issue, in our approach below we will seek independence not between the inferred private and shared latents, but between the private latents of one view and the high-dimensional observations of the other view. These two will only be independent if no shared information has leaked into the putatively private latent.

Different from the above, Mathieu et al. 2016 [32] is a semisupervised approach where pairs of data points within the same class are compared to data points across classes to identify a single encoder decoder pair. While the model is simplified by having only one encoder and decoder, and the model architecture should limit leakage of shared latents into the private, this approach is limited by the class assumptions. First, the data must fall into discrete classes, limiting utility in more continuously varying datasets, and moreover the class of each point is assumed known. Thus this approach is not directly applicable to most neural data.

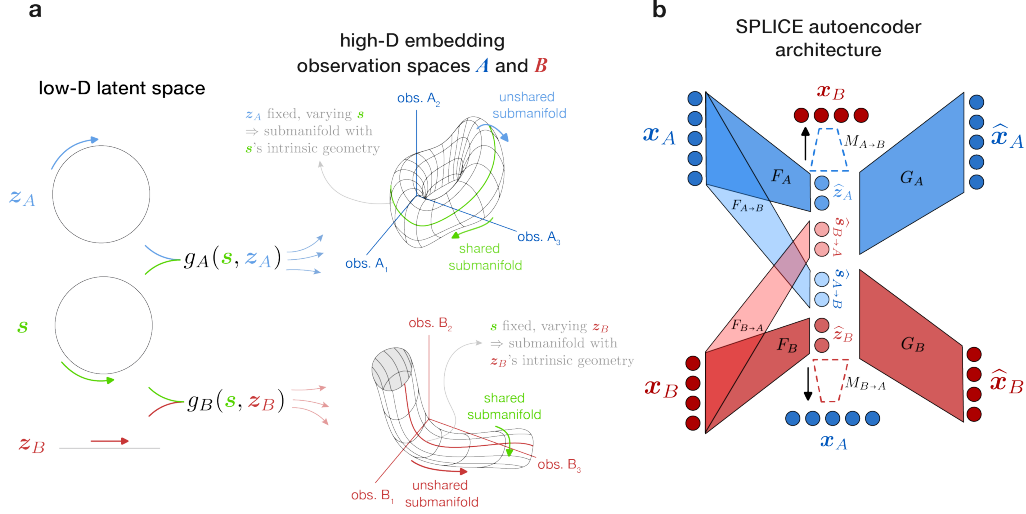


Figure 1: Problem formulation and model architecture. **a)** Illustration of the generative model. Low-dimensional private and shared latent variables are combined nonlinearly to form low-dimensional manifolds embedded in the  $A$  view and  $B$  view high-dimensional observation spaces. **b)** The SPLICE unsupervised autoencoder network architecture.

None of the work we have cited in this section considers the intrinsic geometry of the true shared and private latents, nor do they try to preserve it in the inferred representations. This is a key aspect and we consider related geometry preserving work next.

### 2.2.2 Geometry estimation

Methods that aim to retain geometry are primarily centered around discovering the underlying manifold structure in the data. Often methods considering multi-view data in this space focus on reconstructing a full manifold that is only observed in part, i.e., each view has a portion of the information that must be merged into a global geometry [11, 55, 36]. This approach, while valuable in other applications, cannot address the identification of shared vs. private information within the two views. In essence, they do not address the “partial merge” or the effective “intersection” manifold discovery, instead opting for a “union” manifold discovery.

More similar to our goals is Lederman and Talmon (2018) [28] that use a non-parametric approach to embed a set of data points using diffusion maps. Diffusion maps use a random walk on a correlation-driven graph to define effective geodesic distances between data points. Lederman and Talmon (2018) extend this idea to finding distances between points based on common sources of variation by merging the diffusion operators for the graphs computed separately over each view. This approach, while aiming to identify common geometry, is limited by its non-parametric nature. Specifically, it lacks an explicit representation of the private information in each view, cannot easily embed new points not in the original dataset, and cannot reconstruct data from the latent representation. Additionally, the diffusion framework used to estimate the shared geometry cannot easily be extended to estimate the private geometries, which are also of interest to us.

## 3 Submanifold Partitioning via Least-variance Informed Channel Estimation (SPLICE)

Given two views  $A$  and  $B$ , SPLICE is designed with two features in mind: First, the ability to separate the shared representation of two datasets from each set’s private representations. Second, the ability to preserve the intrinsic geometry of each representation (shared, private to  $A$ , and private to  $B$ ).

### 3.1 Observation model

We begin with our observation model, which characterizes two sets of observable data  $A$  and  $B$  as being generated via two nonlinear functions  $g_A(\cdot)$  and  $g_B(\cdot)$  such that any paired sample  $\mathbf{x}_A \in A \subset \mathcal{R}^{N_A}$  from dataset  $A$  and  $\mathbf{x}_B \in B \subset \mathcal{R}^{N_B}$  from dataset  $B$  can be written as

$$\mathbf{x}_A = g_A(\mathbf{s}, \mathbf{z}_A), \quad \mathbf{x}_B = g_B(\mathbf{s}, \mathbf{z}_B), \quad (6)$$

where  $\mathbf{z}_A, \mathbf{s}, \mathbf{z}_B$  are all independent of each other (Fig. 1a). In these expressions  $\mathbf{s} \in \mathbb{R}^{M_S}$  is a shared set of variables influencing both datasets, while  $\mathbf{z}_A \in \mathbb{R}^{M_A}$  and  $\mathbf{z}_B \in \mathbb{R}^{M_B}$  contribute variability to  $A$  only and  $B$  only, respectively. They are therefore private variables in the sense that, conditioned on the independence of  $\mathbf{z}_A$  and  $\mathbf{z}_B$ ,  $\mathbf{z}_B$  carries no information about  $A$ , and vice versa:

$$I(\mathbf{z}_B; \mathbf{x}_A) = 0, \quad I(\mathbf{z}_A; \mathbf{x}_B) = 0. \quad (7)$$

#### 3.1.1 Strategies to separate the inferred shared latent variables from the private latent variables

Below, to identify these latent spaces, we will separate the inferred shared and private latents using a combination of two strategies: (1) We will guarantee that no private information can leak into the shared latents by using a "crossed butterfly" autoencoder architecture [23]. And (2) we will stop the leakage of shared information into the private latents by using predictability minimization [38] to minimize how well dataset  $A$  can be predicted from the private latents for  $B$ , and vice versa. This will minimize the information that the private latents for one view have about the other view. In other words, it will minimize the shared information in the private latents.

#### 3.1.2 Strategy to identify and preserve the geometry of each group of latent variables

As the set of latent variables vary, they trace out low dimensional manifolds that are embedded in the high dimensional observation spaces (Fig. 1a, right). We note that if we can keep private latents separate from shared latents, then, for either of  $A$  and  $B$ , if one of its latent variables is kept fixed while the other varies, we can, in the observation space, trace out the submanifolds whose geometries we wish to capture. This essentially constitutes a projection of data points onto the desired submanifold.

#### 3.1.3 A two-step process

The second strategy requires successful separation of private and shared latents, meaning that it requires successful completion of the first strategy. Consequently, we will carry out the two strategies in sequence: first we will use an autoencoder architecture to infer latent variables that separate private from shared information. We will then employ these inferred latents to estimate the intrinsic geometries of the underlying private and shared latents. Finally, in a second training step, we will use that information to retrain our autoencoder so as to obtain an updated set of inferred latents that preserve these geometries.

### 3.2 Step 1. Disentangling shared from private representations

To identify the latent spaces we define an autoencoder framework, in a symmetric "crossed butterfly" configuration. Specifically, we define four encoders and two decoders such that each dataset generates both a shared and private set of variables, and is in turn reconstructed from a shared and private set of latents (Fig. 1b). The encoders  $F_A, F_B, F_{A \rightarrow B}, F_{B \rightarrow A}$  and decoders  $G_A, G_B$  are all parameterized as multi-layer neural networks. Given an input data pair  $\mathbf{x}_A$  and  $\mathbf{x}_B$ , the estimated latents are computed as

$$\underbrace{\hat{\mathbf{z}}_A}_{\text{private A latent}} = F_A(\mathbf{x}_A), \quad \underbrace{\hat{\mathbf{z}}_B}_{\text{private B latent}} = F_B(\mathbf{x}_B), \quad \underbrace{\hat{\mathbf{s}}_{B \rightarrow A}}_{\text{shared from B latent}} = F_{B \rightarrow A}(\mathbf{x}_B), \quad \underbrace{\hat{\mathbf{s}}_{A \rightarrow B}}_{\text{shared from A latent}} = F_{A \rightarrow B}(\mathbf{x}_A) \quad (8)$$

and the reconstructed estimates of the inputs are computed as

$$\hat{\mathbf{x}}_A = G_A(\hat{\mathbf{s}}_{B \rightarrow A}, \hat{\mathbf{z}}_A), \quad \hat{\mathbf{x}}_B = G_B(\hat{\mathbf{s}}_{A \rightarrow B}, \hat{\mathbf{z}}_B). \quad (9)$$



The encoders and decoders are trained to reconstruct the inputs  $(\mathbf{x}_A, \mathbf{x}_B)$  by minimizing the mean squared error between  $(\widehat{\mathbf{x}}_A, \widehat{\mathbf{x}}_B)$  and  $(\mathbf{x}_A, \mathbf{x}_B)$  (see below for loss function details). If private information about  $A$  has leaked into the putatively shared latent used to reconstruct  $A$ , optimizing the reconstruction of  $A$  can encourage keeping it there, since reconstruction encourages maximizing information about  $A$  in the latents it is reconstructed from. But the "crossed butterfly" configuration means that the shared latents  $\widehat{\mathbf{s}}_{B \rightarrow A}$  and  $\widehat{\mathbf{s}}_{A \rightarrow B}$  are computed from the dataset they are *not* being used to reconstruct. Consequently, they are guaranteed to carry no private information about the view they are reconstructing, and instead, by construction, can only capture information shared between the two views.

When it comes to the putatively private latents  $\widehat{\mathbf{z}}_A$  and  $\widehat{\mathbf{z}}_B$ , however, the crossed butterfly architecture alone does not ensure that the  $\widehat{\mathbf{z}}_A$  and  $\widehat{\mathbf{z}}_B$  carry only private information. For this we turn to predictability minimization [38].

The central intuition in predictability minimization is that if a variable can be used to predict something about another, there must be non-zero mutual information between the two, and deep networks can be used to estimate predictability. The final two networks we use in our architecture,  $M_{A \rightarrow B}$  and  $M_{B \rightarrow A}$ , which we term "measurement networks," produce predictions of each dataset based on the putative private latent for the other:

$$\mathbf{x}_A^{pred} = M_{B \rightarrow A}(\widehat{\mathbf{z}}_B), \quad \mathbf{x}_B^{pred} = M_{A \rightarrow B}(\widehat{\mathbf{z}}_A). \quad (10)$$

These networks are trained to minimize the mean squared error difference between  $(\mathbf{x}_A^{pred}, \mathbf{x}_B^{pred})$  and  $(\mathbf{x}_A, \mathbf{x}_B)$ . Note that if  $I(\widehat{\mathbf{z}}_B; \mathbf{x}_A) = 0$  then the output of  $M_{B \rightarrow A}(\widehat{\mathbf{z}}_B)$  that minimizes the squared error difference will be the mean  $\bar{\mathbf{x}}_A$  of the dataset  $A$ . This is a constant with regard to the input  $\widehat{\mathbf{z}}_B$ . Thus, with  $\text{Var}[M(\cdot)]$  representing the variance in the output of a network  $M(\cdot)$ , for well-trained measurement networks we have

$$I(\widehat{\mathbf{z}}_B; \mathbf{x}_A) = 0 \Rightarrow \text{Var}[M_{B \rightarrow A}(\widehat{\mathbf{z}}_B)] = 0 \quad \text{and} \quad I(\widehat{\mathbf{z}}_A; \mathbf{x}_B) = 0 \Rightarrow \text{Var}[M_{A \rightarrow B}(\widehat{\mathbf{z}}_A)] = 0. \quad (11)$$

This suggests that  $\text{Var}[M_{B \rightarrow A}(\widehat{\mathbf{z}}_B)]$  and  $\text{Var}[M_{A \rightarrow B}(\widehat{\mathbf{z}}_A)]$  can be used as heuristic terms in the cost functions for the private encoders  $F_B(\cdot)$  and  $F_A(\cdot)$ . The goal is for these terms to encourage those private encoders to produce representations  $\widehat{\mathbf{z}}_B$  and  $\widehat{\mathbf{z}}_A$  that minimize  $I(\widehat{\mathbf{z}}_B; \mathbf{x}_A)$  and  $I(\widehat{\mathbf{z}}_A; \mathbf{x}_B)$ , in which case  $\widehat{\mathbf{z}}_B$  and  $\widehat{\mathbf{z}}_A$  would truly be private latents. However,  $\text{Var}[M_{B \rightarrow A}(\widehat{\mathbf{z}}_B)] = 0 \Rightarrow I(\widehat{\mathbf{z}}_B; \mathbf{x}_A) = 0$  only for binary variables [38]. For analog variables and optimally trained, arbitrarily expressive measurement networks, minimizing their output variance will produce only the two conditions on the right of equation (12), which we refer to as "first-order independence":

$$\begin{aligned} \text{Var}[M_{B \rightarrow A}(\widehat{\mathbf{z}}_B)] = 0 &\Rightarrow L_A(\widehat{\mathbf{z}}_B) \equiv \mathbb{E}[\mathbf{x}_A | \widehat{\mathbf{z}}_B] = \text{const.} \\ \text{Var}[M_{A \rightarrow B}(\widehat{\mathbf{z}}_A)] = 0 &\Rightarrow L_B(\widehat{\mathbf{z}}_A) \equiv \mathbb{E}[\mathbf{x}_B | \widehat{\mathbf{z}}_A] = \text{const.} \end{aligned} \quad (12)$$

In other words, the functions  $L_A(\widehat{\mathbf{z}}_B)$  and  $L_B(\widehat{\mathbf{z}}_A)$  being constants imply that there is no mutual information between  $\widehat{\mathbf{z}}_B$  and the first moment of  $\mathbf{x}_A$ , or between  $\widehat{\mathbf{z}}_A$  and the first moment of  $\mathbf{x}_B$ . Note that first-order independence between  $\mathbf{x}$  and  $\mathbf{z}$  is a condition much stronger than simply decorrelation of  $\mathbf{x}$  and  $\mathbf{z}$ , as it is a condition on the first-order moment of  $\mathbf{x}$  for each and every value of  $\mathbf{z}$ , whereas decorrelation is an average over all  $\mathbf{z}$ . For example, for a distribution composed of the data points  $(z, x) = (-1, 1), (1, -1), (2, 0.5), (-2, -0.5)$ , the variables  $x$  and  $z$  are uncorrelated, but  $x$  is not 1st-order independent from  $z$ .

In this terminology,  $N^{\text{th}}$ -order independence between  $\mathbf{x}$  and  $\widehat{\mathbf{z}}$  would be the condition  $L^{(N)}(\widehat{\mathbf{z}}) \equiv \mathbb{E}[\mathbf{x}^N | \widehat{\mathbf{z}}] = \text{const.}$  If  $\mathbf{x}$  is  $i^{\text{th}}$ -order independent from  $\mathbf{z}$  for all  $i = 1 \dots N$ , and  $N \rightarrow \infty$ ,  $\mathbf{x}$  will become fully independent from  $\mathbf{z}$ , since all its moments will be independent from  $\mathbf{z}$  and therefore its distribution will be independent from  $\mathbf{z}$ . Guaranteeing first-order independence can therefore be thought of as akin to guaranteeing a first-order approximation to independence. Surprisingly, in our experiments below, we have found that first-order independence appears sufficient to lead networks towards solutions that also seem to satisfy full statistical independence (i.e.,  $N^{\text{th}}$ -order independence for all  $N$ ; see Supp. Figs. 1a, 1b, 2b, 2c and see Discussion for how to check for higher order independence, and correct for it if necessary).

In summary, we aim to minimize the reconstruction loss terms  $\mathcal{L}_{rec}^A$  and  $\mathcal{L}_{rec}^B$

$$\mathcal{L}_{rec}^A = \|\mathbf{x}_A - G_A(\widehat{\mathbf{s}}_{B \rightarrow A}, \widehat{\mathbf{z}}_A)\|_2^2, \quad \mathcal{L}_{rec}^B = \|\mathbf{x}_B - G_B(\widehat{\mathbf{s}}_{A \rightarrow B}, \widehat{\mathbf{z}}_B)\|_2^2, \quad (13)$$

while also minimizing the variance in the measurement networks’ outputs. Consequently, the autoencoder networks  $\theta_{ae} = \{G_A, G_B, F_A, F_B, F_{A \rightarrow B}, F_{B \rightarrow A}\}$  will be optimized according to

$$\begin{aligned} \mathcal{L}_{SPLICE} &= \mathbb{E} [\mathcal{L}_{rec}^A + \mathcal{L}_{rec}^B + \text{Var} [M_{A \rightarrow B}(\hat{\mathbf{z}}_A)] + \text{Var} [M_{B \rightarrow A}(\hat{\mathbf{z}}_B)]] \\ \theta_{ae}^* &= \arg \min_{\theta_{ae}} \mathcal{L}_{SPLICE} \end{aligned} \quad (14)$$

The loss function above depends on having the best possible set of predictors  $\theta_{pred} = \{M_{A \rightarrow B}, M_{B \rightarrow A}\}$ . We thus continuously update the measurement networks to minimize their prediction losses

$$\mathcal{L}_{pred}^A = \|\mathbf{x}_A - M_{B \rightarrow A}(\hat{\mathbf{z}}_B)\|_2^2 \quad \mathcal{L}_{pred}^B = \|\mathbf{x}_B - M_{A \rightarrow B}(\hat{\mathbf{z}}_A)\|_2^2. \quad (15)$$

so that

$$\theta_{pred}^* = \arg \min_{\theta_{pred}} \mathbb{E} [\mathcal{L}_{pred}^A + \mathcal{L}_{pred}^B] \quad (16)$$

---

**Algorithm 1** Training process for Step 1, separating shared and private latents

---

- 1: Initialize autoencoder networks  $\theta_{ae} = \{G_A, G_B, F_A, F_B, F_{A \rightarrow B}, F_{B \rightarrow A}\}$
  - 2: Initialize measurement networks  $M_{A \rightarrow B}$  and  $M_{B \rightarrow A}$
  - 3: **for**  $i$  in  $1 \dots n_{iter}$  **do**
  - 4:   Encode inputs  $\mathbf{x}_A$  and  $\mathbf{x}_B$  to get all latents:  $\hat{\mathbf{s}}_{B \rightarrow A}$  and  $\hat{\mathbf{s}}_{A \rightarrow B}$ ,  $\hat{\mathbf{z}}_A$  and  $\hat{\mathbf{z}}_B$
  - 5:   Decode shared and private latents to reconstruct inputs:  $\hat{\mathbf{x}}_A$  and  $\hat{\mathbf{x}}_B$
  - 6:   Compute reconstruction loss  $\mathcal{L}_{rec}^A$  and  $\mathcal{L}_{rec}^B$
  - 7:   Compute  $\text{Var} [M_{B \rightarrow A}(\hat{\mathbf{z}}_B)]$  and  $\text{Var} [M_{A \rightarrow B}(\hat{\mathbf{z}}_A)]$
  - 8:   Update encoder and decoder networks to minimize  $\mathcal{L}_{rec}^A$  and  $\mathcal{L}_{rec}^B$
  - 9:   Update encoder networks to minimize  $\text{Var} [M_{B \rightarrow A}(\hat{\mathbf{z}}_B)]$  and  $\text{Var} [M_{A \rightarrow B}(\hat{\mathbf{z}}_A)]$
  - 10:   **if**  $i \bmod T_{restart} = 0$  **then**
  - 11:     Restart measurement networks
  - 12:      $n_{msr} = 1000$
  - 13:   **else**
  - 14:      $n_{msr} = 5$
  - 15:   **end if**
  - 16:   **repeat** for  $n_{msr}$  iterations
  - 17:     Use measurement networks to predict datasets from private latents:  $\mathbf{x}_A^{pred}$  and  $\mathbf{x}_B^{pred}$
  - 18:     Compute measurement networks’ prediction loss  $\mathcal{L}_{pred}^A$  and  $\mathcal{L}_{pred}^B$
  - 19:     Update measurement networks to minimize  $\mathcal{L}_{pred}^A + \mathcal{L}_{pred}^B$
  - 20:   **until** end of  $n_{msr}$  iterations
  - 21: **end for**
- 

Successful training will produce an autoencoder that reproduces its inputs while separating private and shared latent information.<sup>1</sup>

**SPLICE Model fitting** To fit the multiple, interacting networks comprising the SPLICE model, we adopt an alternating optimization approach using backpropagation [38]. For each training iteration, we proceed in three steps (see algorithm 1). We first take a gradient step to minimize the joint reconstruction loss  $\mathcal{L}_{rec} = \mathcal{L}_{rec}^A + \mathcal{L}_{rec}^B$  over all encoders and decoders. Next we take a gradient step to minimize the measurement prediction variances  $\text{Var} [M_{A \rightarrow B}(\hat{\mathbf{z}}_A)]$  and  $\text{Var} [M_{B \rightarrow A}(\hat{\mathbf{z}}_B)]$  over the corresponding private encoder. Finally, we take multiple gradient steps (the number is a hyperparameter) to minimize the measurement prediction losses  $\mathcal{L}_{pred} = \mathcal{L}_{pred}^A + \mathcal{L}_{pred}^B$  over the measurement networks.

Taking multiple gradient steps to minimize  $\mathcal{L}_{pred}$  for each single step of the other losses ensures that the measurement networks are well-trained. Because the effectiveness of our disentangling strategy relies on the measurement networks being well-trained and able to learn complex relationships, we use measurement networks that are as wide and deep as the decoder networks, and periodically cold restart them to avoid local minima.

<sup>1</sup>It has been noted [19] that training of the measurement networks is different, but closely related, to Generative Adversarial Networks (GANs): the  $M(\cdot)$  network aims to improve its prediction of a data set, while the  $F(\cdot)$  network that provides  $M$ ’s input aims to hinder this prediction.

### 3.3 Step 2. Preserving intrinsic geometries.

In this second step, we aim to find latent representations  $\hat{z}_A, \hat{s}_{A \rightarrow B}, \hat{s}_{B \rightarrow A}, \hat{z}_B$  that preserve the intrinsic data geometries of the underlying private and shared latents. By this we mean that Euclidean distances in the inferred latent representations will approximately match the corresponding submanifold’s geodesic distances. Critically, having separated private and shared latents in Step 1 allows estimating the geodesic distances for each latent group separately from the others. To do this, we first use a trained SPLICE network to trace out, in the observed data spaces, data points lying on a submanifold corresponding to each latent (Fig. 1a, right). We then follow the methods of [43] to estimate geodesic distances between pairs of points along each of those submanifolds. Finally, we retrain our SPLICE network, while incorporating a loss term that is minimized when Euclidean distances between pairs of points in the inferred latent spaces match the estimated geodesic distances for the corresponding pair of points in the observation spaces.

We note that successful completion of Step 1 implies that, in the limit of large number of training data points, for data points in the training set, the distributions of the corresponding samples of  $\hat{s}_{B \rightarrow A}$  and  $\hat{z}_A$  will be approximately independent of each other, since the two will have been disentangled. This means that the reconstructed data points  $\hat{x}_A = G_A(\hat{s}_{B \rightarrow A}, \hat{z}_A)$  will be distributed as the cross product of the data distribution of each of those two latents, passed through the decoder  $G_A()$ . If the reconstruction loss is low, the reconstructed points  $\hat{x}_A$  will lie approximately on the data manifold for  $x_A$ . Importantly, it then follows that holding one of the latents fixed, while varying the other latent using values from the data distribution, and using  $G_A()$  to project these latents into the observation space, will produce points that are on the data manifold itself. Moreover, they will be constrained to be on a submanifold of the data manifold that has the intrinsic geometry of the latent that is being varied (Fig. 1a, right). We can therefore use the set of points constructed in such a manner to estimate geodesic distances along the submanifolds, and therefore gain insight into the intrinsic geometry for each of the latents.

For example, to obtain an example of the  $z_A$  submanifold, we randomly choose one of the values of  $\hat{s}_{B \rightarrow A}$  in the data set, set  $\hat{s}_{B \rightarrow A}^{fix}$  to that value, and compute

$$\hat{x}_A^{z_A \text{ submanifold}} = G_A\left(\hat{s}_{B \rightarrow A}^{fix}, F_A(x_A)\right). \quad (17)$$

This is a reconstruction of  $x_A$  while keeping  $\hat{s}_{B \rightarrow A}$  fixed at a random point. (In practice, we replace each data point  $\hat{x}_A^{z_A \text{ submanifold}}$  with the average of its local neighborhood to reduce noise.) We then measure geodesic distances between each pair of reconstructed points along the submanifold using the approach of [43]: a local nearest neighbor group is found for each point, and then geodesic distances between all pairs of points are estimated using Dijkstra’s algorithm. (In practice, we use the approach from Landmark Isomap [40], which scales better for high dimensional data.) We refer to the geodesic distances between pairs of points that are computed in this manner as  $D_A^{geo}$ . We refer to corresponding Euclidean distances in the inferred latent space  $\hat{z}_A$  as  $D_A^z$ . We then compute a loss that is the square root of the mean, over all pairs of data points, of the squared differences between  $D_A^z$  and  $D_A^{geo}$ :  $\mathcal{L}_A^{geo} = \sqrt{\|D_A^z - D_A^{geo}\|_2}$ . This loss will be minimized when  $D_A^z$  are the same as  $D_A^{geo}$ . We thus refer to it as a "geometry-preserving loss." A similar process is used to compute a geometry-preserving loss for each of the inferred latent spaces,  $\mathcal{L}_{B \rightarrow A}^{geo}, \mathcal{L}_{A \rightarrow B}^{geo}, \mathcal{L}_A^{geo}, \mathcal{L}_B^{geo}$ .

Finally, we retrain the SPLICE network with these loss terms added to the autoencoder loss from Equation (14), such that the optimal autoencoder parameters  $\theta_{ae}^*$  become

$$\theta_{ae}^* = \arg \min_{\theta_{ae}} [\mathcal{L}_{SPLICE} + \mathcal{L}_{B \rightarrow A}^{geo} + \mathcal{L}_{A \rightarrow B}^{geo} + \mathcal{L}_A^{geo} + \mathcal{L}_B^{geo}]. \quad (18)$$

During each re-training epoch, the Euclidean distances in the latent spaces are recomputed, but the geodesic distances are computed only once before re-training begins.

## 4 Experiments

**Experiment 1: Rotated MNIST.** To investigate SPLICE’s ability to disentangle private and shared sources of variance in high-dimensional data with realistic variation, we turned to MNIST images. Dataset  $A$  consisted of the original MNIST digits and the paired dataset  $B$  consisted of a random rotation of each of  $A$ ’s digits, with the rotation angle sampled uniformly from 0 to 360 degrees

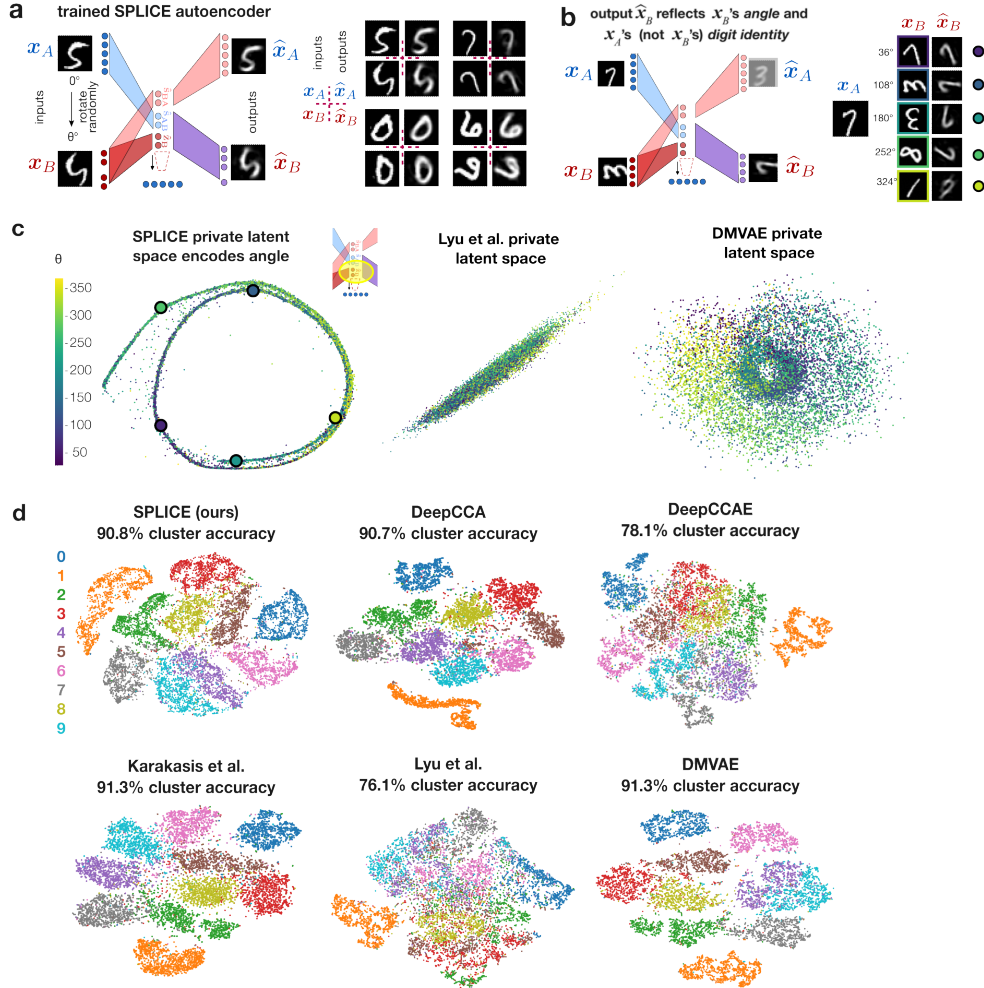


Figure 2: Rotated MNIST digit example. **a)** During training,  $A$  view inputs are original MNIST digits,  $B$  view inputs are a random rotation of them. **b)** The  $B$  view private latent learns to encode the rotation angle. **c:** (left) The  $F_B(\cdot)$  private encoder in SPLICE distills from input  $x_B$  only the rotation angle, and discards digit identity. SPLICE retains the circular angle geometry, unlike Lyu et al. [31] and DMVAE. **d)** tSNE visualization of clusters in the shared spaces in SPLICE shows that SPLICE successfully separates digits into distinct clusters. Competing methods tend to have less clear clusters (e.g., DeepCCAe and Lyu et al.) and at best comparable clustering (DeepCCA, Karkasis et al., and DMVAE) as measured by the classification accuracy.

(Fig. 2a). We used 50k unique images for training and 10k images for hyperparameter validation, and 10k images for evaluate test performance, with a single random rotation of each digit.

By construction, the information shared between  $A$  and  $B$  during training is the digit identity (0, 1, 2, ... etc.) and other digit-specific features (e.g. line thickness), while the information private to  $B$  is exclusively the rotation angle. Since the  $x_A$  inputs were left unrotated, there was no private information for  $A$  and we thus did not use include here a private  $A$  encoder  $F_A(\cdot)$ . We fit a SPLICE architecture with 30 units for each of the inferred shared latents  $\hat{s}_{A \rightarrow B}$  and  $\hat{s}_{B \rightarrow A}$ , and 2 units for the inferred private latent  $\hat{z}_B$ , since preserving the geometry of a 1D circular variable (angle) requires two linear dimensions. Encoder, decoder, and measurement networks each consisted of 4 hidden layers with sizes [256, 128, 64, 32]. Two features of the dataset are worth noting: First, while we expect SPLICE to identify the rotational private latent space, symmetric digits such as 0, 1, and 8, together with the indistinguishability of sixes and 180°-rotated nines, lead us to expect that the geodesic distance between angles 180° apart should not be large. Second, some MNIST digits are naturally tilted, even while all originals are labeled as being 0° w.r.t. the original.

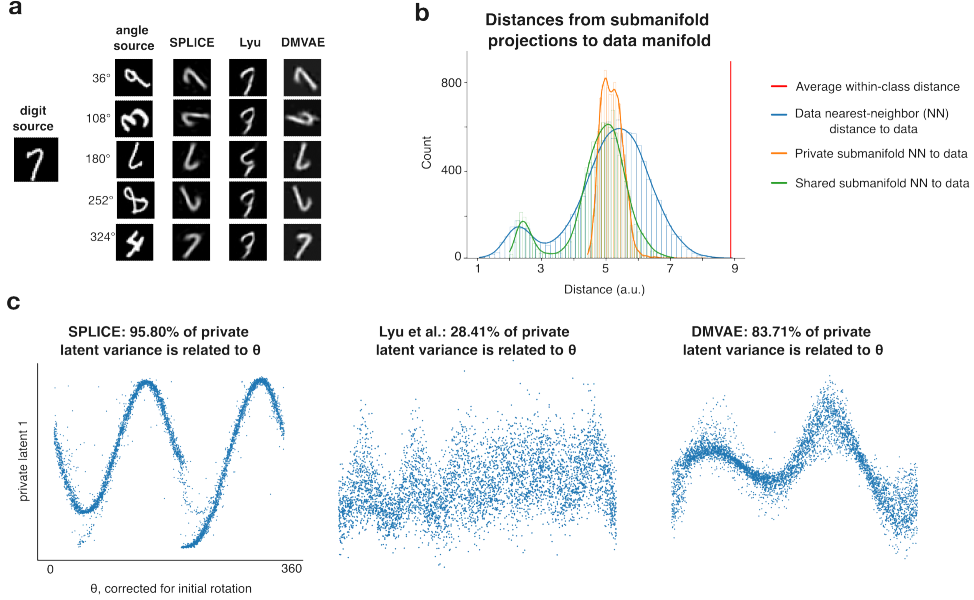


Figure 3: MNIST Rotation example: learned private geometry. **a)** Example rotated digits generated by using the shared latent variable from the digit source (in this case a "7") and the private latent from an angle source for several angles. SPLICE accurately reconstructs the rotated "7" using the reconstruction networks for all angles. Lyu et al. has worse reconstructions across angles, despite being able to reconstruct digits accurately from unperturbed shared and latent variables from the same digit (digit source = angle source). DMVAE better reconstructs the rotated digits in most cases, but it sometimes fails to correctly interpret the rotation angle from the latents (e.g., the 108 degree rotation in the second row). **b)** Analysis of distances quantifying how closely the learned latents represent the original data manifold. Distances between the private and shared submanifolds (i.e. rotated digits) show distributions similar to the distribution nearest-neighbors distances between observed data points. The smaller distances, when compared to the average within-digit-class distance indicates that the projections lie on the original data manifold. **c)** Quantification of the private latent variables in terms of which percent of internal variance represents the private rotation information. SPLICE (left) displays a tight, one-dimensional trace oscillating with the rotation angle in a sinusoidal pattern. This accurately represents the latent angle, with 95.8% of variance being accounted for by the rotation angle  $\theta$  (see methods). Lyu at al. (middle, 28.41% variance related to  $\theta$ ) and DMVAE (right, 83.71% variance related to  $\theta$ ) contain significant fluctuations unrelated to the rotation angle, indicating bleedthrough of shared information in the private space.

The fit SPLICE model performed well as an autoencoder, accurately reconstructing the original and rotated digits (Fig. 2a). The inferred private latent  $\hat{z}_B$  was consistent with our expectations, with data points largely arranged along a 1D manifold (Fig. 2c). This manifold, along which rotation angle steadily increased, was approximately a double-circle, which allowed angles 180° apart to be relatively nearby in the latent space.

Remarkably, the disentangled latent space allowed us to generalize and generate arbitrarily rotated images of digits for digit-angle combinations not in the training set. Given the crossed architecture, if the private encoder  $F_B(\cdot)$  truly distills only rotation angle, the reconstruction  $\hat{x}_B$  should retain input  $x_B$ 's rotation angle, but discard all of  $x_B$ 's digit-specific features, replacing them with those from input  $x_A$ . To test this, we provided different digits as inputs  $x_A$  and  $x_B$ . Indeed, the output  $\hat{x}_B$  reflected  $x_A$ 's digit identity, but with a rotation angle specified by  $x_B$  (Fig. 2b). To quantify whether these projections lie on the original data manifold, we calculated the distances between the private submanifold (i.e. the arbitrarily rotated digits) and the nearest-neighbors in the observed dataset, and repeated a similar calculation for the shared submanifold. For both submanifolds, the distributions of submanifold nearest-neighbors distances were similar to the distribution nearest-neighbors distances between observed data points. Virtually all projection nearest-neighbors distances were smaller

than the average within-digit-class distance. Taken together, these distance metrics suggest that the projections do in fact lie on the original data manifold (Fig 3b).

Both shared latent spaces  $\hat{s}_{A \rightarrow B}$  and  $\hat{s}_{B \rightarrow A}$  showed clear organization by digit, with clusters for similar digits (e.g. 4 and 9, 3 and 8) appearing closer together (Fig. 2d), and no apparent representation of angle (Supp. Fig. 1). To quantify the quality of the shared latent space, we used a linear support vector machine to predict the digit labels of each sample from its shared latents. SPLICE showed comparable accuracy to the best competing methods (DeepCCA, Karakasis et al., and DMVAE). Notably, the two uncrossed deterministic autoencoding (DeepCCA and Lyu et al.) methods produce latent spaces that are visibly disorganized and result in significantly worse clustering.

In addition to matching the state-of-the-art in shared latent estimation, SPLICE outperforms the competing methods in private estimation. While SPLICE correctly extracts a 1D circular latent variable with clear correspondence to angle (Fig. 2c, left), Lyu et al. produces a latent space with no clear organization by rotation angle (Fig. 2c, middle). We suspect that the Lyu et al. model had considerable leakage of shared information into the private space and vice versa, resulting in no clear angle encoding in the private latent space. This is further supported by the inability of the Lyu et al. model to compose digit identity and angles from different test samples (Fig 3a). While the DMVAE model shows visible organization by angle, it fails to extract a 1d circular manifold, and instead produces a circular point cloud, presumably due to its isotropic Gaussian prior on the latent space. Although the DMVAE model is better at composing the shared and private latents from different samples, the disorganization of the private latent space sometimes results in an incorrect rotation angle (Fig. 3a, second row).

To quantify how much of the private latent variance is related to rotation angle, we first corrected for the inherent rotation angle in the MNIST dataset, and then used a narrow sliding window to compute private latent variance conditioned on rotation angle (see Supplement for details). From this metric and from scatter plots of the private latent vs rotation angle (Fig. 3c), SPLICE clearly outperforms Lyu et al. and DMVAE in private-shared separation; SPLICE displays a tight 1D sinusoid with almost all the variance being explained by rotation angle, while Lyu et al. and DMVAE exhibit considerable fluctuations unrelated to the rotation angle.

Our results on this dataset demonstrate that SPLICE estimates shared latents as well as competing methods and outperforms competing methods in terms of private-shared separation. Additionally, the geometry-preservation allows the SPLICE private to be easily interpreted as a 1D circular variable, while the private latents of the other space are not as readily interpretable. Overall, SPLICE can cleanly separate private and shared information across two views in an unsupervised manner, and can find low-dimensional and interpretable representations of high-dimensional multi-view data.

**Experiment 2: Synthetic LGN-V1 activity.** Motivated by applications in neuroscience, we probed SPLICE’s ability to handle nonlinear, noisy, neural-like data by simulating data representing noisy visual system responses for which ground truth information was known. Specifically, given a stimulus consisting of a bar of light presented at different positions in different trials, datasets  $A$  and  $B$  are the activity of a field of simulated LGN neurons and V1 neurons, respectively. The stimuli were kept at a single orientation (vertical). By construction, the ground truth shared information across both views is the X and Y position of the bar, which geometrically is a 2-dimensional sheet. The LGN population consisted of 400 neurons, with center-surround receptive fields whose centers were evenly spaced on a two-dimensional 20x20 grid. The V1 population consisted of two evenly spaced 20x20 grids of neurons with Gabor filter receptive fields (i.e., V1 was 800-dimensional). The first grid had vertically oriented Gabor filters and the second had horizontally oriented Gabor filters. The visual field was implemented as a 100x100 pixel grid, and the size of each neuron’s receptive field was 30x30 pixels.

In addition to the shared visual stimulus, each population also responded to a private 1-D stimulus. For each population, this was generated by placing a virtual agent along a 1-D virtual linear track. Each neuron had a randomly centered Gaussian place field on this linear track. On different trials, the LGN agent and the V1 agent were placed at random, mutually independent, positions on the track. The neuronal responses to the shared and private stimuli were added linearly to obtain the final activity for each neuron. We scaled the variance of the responses to the private latents to be 6X the variance of responses to shared latents. Fig. 4a shows example stimuli and inputs to the SPLICE network in Fig. 4b show an example of the resulting LGN and V1 population activity. In some simulations, we also added i.i.d. noise to each individual neuron. For each simulation, we generated 18,900 trials, with the stimulus placed at a randomly chosen X and Y position for each

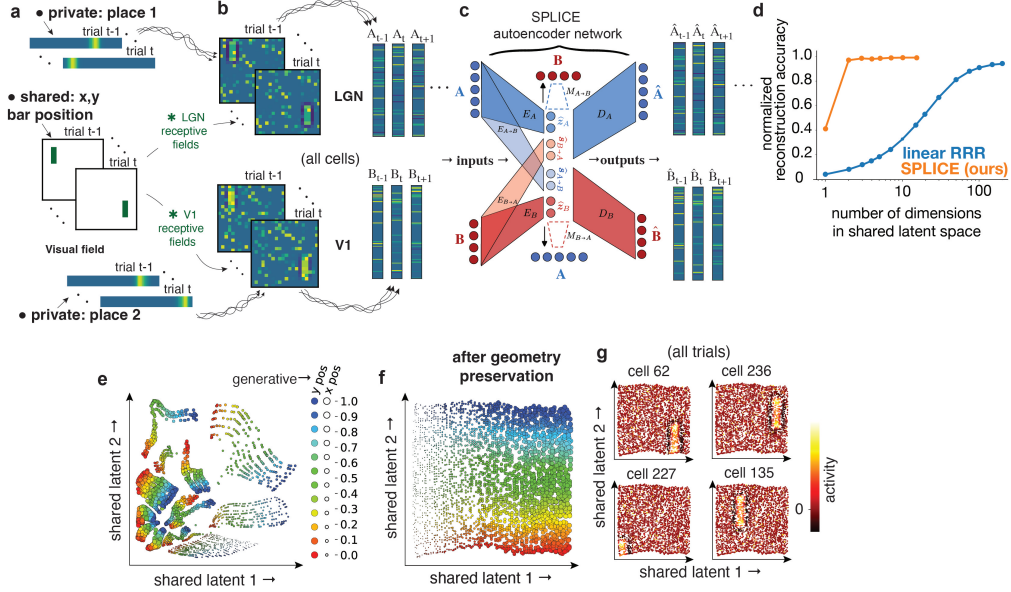


Figure 4: Simulated LGN-V1 experiments. **a**) Three independent types of data are multiplexed across two synthetic brain regions: a location on a linear track (place 1, private to region A), the  $x, y$  position of a vertical bar used as a visual stimulus (shared across regions A and B), and a second location on a second linear track (place 2, private to region B) **b**) The visual stimulus drives center-surround receptive fields, with their centers tiling the visual space in region A; region B was similar but had oriented receptive fields. For this view, the neurons have been ordered according to their visual receptive field centers. But the neurons’ private place order is unrelated to their visual field centers, so in this view the place activity appears as random noise. To maximally challenge our network we further corrupted responses with i.i.d. noise. **c**) The SPLICE network has access to neither the visual field ordering nor the place field ordering of the neurons. On each trial, it receives only a vector of activities for each region. Nearby elements in these vectors are not necessarily neurons with nearby visual or place fields. **d**) SPLICE autoencoder network. **e**) Following “RRR” (Semedo 2019), we estimate the dimensionality of the shared latents as the dimension at which the autoencoder’s reconstruction accuracy saturates. SPLICE estimates this as  $d=2$ , the correct ground truth. RRR, the current gold standard in systems neuroscience, severely overestimates it as  $d=70$ . **f**) Value of the shared latents for each trial (each dot is one trial) for the 2-d SPLICE network, before applying geometry preservation. The data structure is difficult to interpret. **g**) Same as **f**, but after applying geometry preservation. Even without having any knowledge of the existence of a visual field, geometry preservation has allowed SPLICE to arrange the data into an interpretable 2-d field. Since we know the ground truth for these synthetic data, we can label the trials by the  $x$  and  $y$  position of the visual stimulus in that trial (dot size and dot color, respectively). This shows that the axes in the estimated latent space correspond to the  $x$ - and  $y$ - axes of the visual field. **h**) Each panel shows the data as in **g**, but now colored by the activity of a randomly chosen neuron: SPLICE allows discovering that the activity coordinated across the regions has localized receptive fields that tile the shared space.

trial. 80% of the trials were used for training, and the remaining 20% were used for the testing results shown in Fig. 4.

We fit SPLICE networks with different numbers of units in the latent spaces, and found that SPLICE accurately reconstructed neural activity (example reconstruction in Fig. 4b). Reduced Rank Regression (RRR) [39], a comparable but linear state-of-the-art method in neuroscience, estimates dimensionality of shared spaces by using gradually increasing dimensionality and identifying when reconstruction quality saturates. We following the same approach, and found that SPLICE correctly identified the true generative shared dimensionality ( $n_s = 2$ ; Fig. Fig. 4c, orange). In contrast, RRR required  $\approx 75$  dimensions for reconstruction to saturate (Fig. 4c, blue).

Although the geometry-preserving step 2 did not change reconstruction quality (not shown), it had substantial impact on the geometry of the latent representations (compare Fig. 4d and e). After

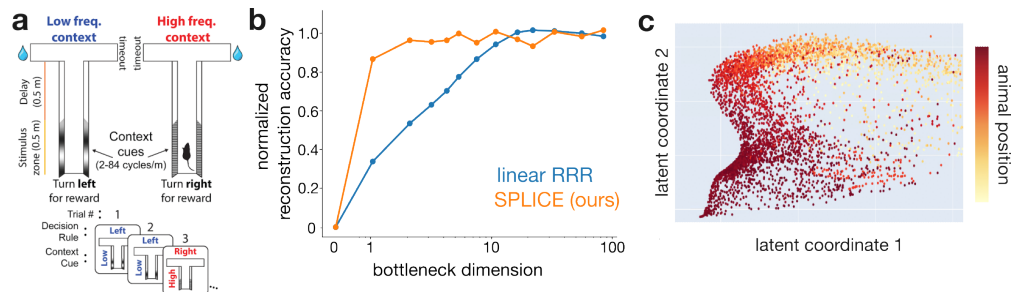


Figure 5: SPLICE and experimental neurophysiological data. **a)** On each trial, mice made a Left/Right decision on a virtual T-maze. The correct response was cued by a visual stimulus in the first half of the stem of the T. Simultaneous recordings yielded 96 neurons in hippocampus, and 348 neurons in medial prefrontal cortex. **b)** SPLICE outperformed RRR [39], summarizing the shared space in 2 dimensions, instead of 12. **c)** The shared latent space encodes the animal’s position along the maze.

the geometry-preserving step 2, the data in the shared latent space were cleanly arranged in a two-dimensional sheet whose axes corresponded to the ground truth X and Y position (Fig 4e), illustrating how our unsupervised approach can generate interpretable latent geometries.

Fitting a nonlinear method, DeepCCA [1], to the same simulated data produced a shared space that distorted information about Y position and discarded most information about stimulus X position. This contrasts with SPLICE, whose reconstruction loss term requires the network to preserve shared information (such as stimulus X position) that accounts for variance in the data.

### Experiment 3: Data from neurophysiological experiments.

Finally, we turned to experimental neurophysiological data, and asked how SPLICE would compare to state-of-the-art methods in finding and summarizing information shared across two brain regions. We fit SPLICE to electrophysiologically-recorded neural data from simultaneous Neuropixels recordings of hippocampus and prefrontal cortex, taken as mice performed a decision making task in a Virtual Reality T-maze (Fig. 5a). SPLICE outperformed Reduced Rank Regression [39] in that reconstruction quality saturated with just two dimensions, while RRR required  $\approx 12$  for reconstruction to saturate (Fig. 5b). The inferred latent space showed a shared encoding of the animal’s position (Fig. 5c), consistent with the presence of place cells in both brain regions.

## 5 Discussion

In this work we present the SPLICE autoencoder architecture to (a) identify and disentangle shared and private low-dimensional latent spaces underlying two distinct views of the same system; (b) maximally capture variance in the data sets; and (c) find shared and private latent spaces that preserve intrinsic geometry, in the sense that Euclidean distances in the latent spaces best match geodesic distances in the intrinsic data geometry. We propose SPLICE as an approach for generating, in an unsupervised manner, succinct and interpretable summaries of complex, high-dimensional paired data sets. Our approach outperforms existing nonlinear methods such as deepCCA [1] as well as linear methods such as reduced rank regression [39].

Prior work on disentangling has focused on completely disentangling every latent variable from all others [38, 25, 29]. This modeling choice can distort geometrical shapes, for example circular latents cannot be modeled by two independent variables. Our model removes this requirement within each of the shared and private spaces to enable the learning of the data geometry in each space.

In this work we defined  $N^{th}$ -order independence such that  $y$  being  $N^{th}$ -order independent from  $z$  implies that the function  $L(z)\mathbf{E}_y(y^N|z)$  is a constant. In other words, there is no mutual information between  $z$  and the  $N^{th}$  moment of  $y$ . For  $N=1$  this is a much stronger condition than decorrelation, as it is a condition on the first-order moment of  $y$  for each and every value of  $z$ , whereas decorrelation is an average over all  $z$ . For example, with a distribution composed of the data points  $(z, y) \in \{(-1,1), (1,-1), (2,0.5), (-2,-0.5)\}$ ,  $y$  and  $z$  are decorrelated, but  $y$  is not  $1^{st}$ -order independent from  $z$ . Although stronger than decorrelation, indeed  $1^{st}$ -order independence is not full independence. Future work can extend the SPLICE framework by constraining higher order independence, which may be required for more complex data.



The choice of basing SPLICE on an autoencoder framework rests on wanting to preserve precise geometry via the pairwise distances loss  $\mathcal{L}^{geo}$ . Alternate architectures and losses based on variational autoencoders (VAEs) may be possible, and methods exist that target independence in the latent layers of VAEs [14]. However, such models would require significant additional changes to enable the factorized posterior approximations to learn more complex geometry.

Another important consequence of using the autoencoder framework is the ability to reconstruct and thus 1) quantify variance explained 2) easily embed new points outside of the original dataset. Quantifying reconstruction errors is important in ensuring goodness of fit for the embeddings when the data represents complex measurements with unknown geometry. Embedding new points similarly enables ongoing observations to be analyzed using the learned representation. These benefits are unfortunately not easily achievable by non-parametric methods, such as that proposed using diffusion maps [28].

To optimize SPLICE we took a two-stage approach, first optimizing the disentangling of shared and private information and then learning each sub-manifold’s geometry. While a single end-to-end training procedure would be much more concise and aesthetic, such an approach would end up using imperfectly disentangled data to learn the geometry, and then the resulting imperfect geometry to back propagate erroneous information into the disentangling network. We avoid this potential lack of convergence as we always want the predictor network to be maximally accurate, and so we prioritize first allowing it to train to completion before introducing the geometry piece.

Beyond the examples here where we focus on two datasets with roughly the same qualities (e.g., two images, or two populations of neurons), SPLICE has the capacity to extend further, e.g., to matching brain data with quantitative behavioral measurements from video data. Thus we believe SPLICE can be a more general purpose analysis tool across applications.

**Limitations:** One of the current primary limitations of SPLICE is that it can only account for two views at once. Analyzing three or more would require pair-wise runs of SPLICE on each pair of views. This limitation, while seemingly restrictive, is likewise faced by CCA, and all extensions or generalizations thereof. A second limitation of SPLICE is the omission of temporal dynamics. Splice specifically targets the geometry, and not the temporal evolution of the data. Future work should consider the power of combining these approaches. Finally, we limit SPLICE to minimizing the first-order independence. While we found this constraint computationally efficient and sufficient for our applications, new applications should check that higher-order independence holds after training SPLICE, and potentially adjust the cost function if needed.

## References

- [1] Galen Andrew, Raman Arora, Jeff Bilmes, and Karen Livescu. Deep canonical correlation analysis. In Sanjoy Dasgupta and David McAllester, editors, *Proceedings of the 30th International Conference on Machine Learning*, volume 28 of *Proceedings of Machine Learning Research*, pages 1247–1255, Atlanta, Georgia, USA, 2013. PMLR.
- [2] Ricard Argelaguet, Anna SE Cuomo, Oliver Stegle, and John C Marioni. Computational principles and challenges in single-cell data integration. *Nature biotechnology*, 39(10):1202–1215, 2021.
- [3] Edoardo Balzani, Jean Paul Noel, Pedro Herrero-Vidal, Dora E Angelaki, and Cristina Savin. A probabilistic framework for task-aligned intra- and inter-area neural manifold estimation. *arXiv [q-bio.NC]*, September 2022.
- [4] K Barber, H Kim, F M Traub, B Chen, and A Vaziri. High-speed, cortex-wide volumetric recording of neuroactivity at cellular resolution using light beads microscopy. *Nature*, 2021.
- [5] Rishidev Chaudhuri, Berk Gerçek, Biraj Pandey, Adrien Peyrache, and Ila Fiete. The intrinsic attractor manifold and population dynamics of a canonical cognitive circuit across waking and sleep. *Nat. Neurosci.*, 22(9):1512–1520, September 2019.
- [6] Benjamin Culpepper and Bruno Olshausen. Learning transport operators for image manifolds. *Advances in neural information processing systems*, 22, 2009.
- [7] John P Cunningham and Zoubin Ghahramani. Linear dimensionality reduction: Survey, insights, and generalizations. *The Journal of Machine Learning Research*, 16(1):2859–2900, 2015.
- [8] Sadegh Ebrahimi, Jérôme Lecoq, Oleg Rumyantsev, Tugce Tasci, Yanping Zhang, Cristina Irimia, Jane Li, Surya Ganguli, and Mark J Schnitzer. Emergent reliability in sensory cortical coding and inter-area communication. *Nature*, 605(7911):713–721, May 2022.
- [9] S A Engel, D E Rumelhart, B A Wandell, A T Lee, G H Glover, E J Chichilnisky, and M N Shadlen. fMRI of human visual cortex. *Nature*, 369(6481):525, June 1994.
- [10] Sudeep Fadadu, Shreyash Pandey, Darshan Hegde, Yi Shi, Fang-Chieh Chou, Nemanja Djuric, and Carlos Vallespi-Gonzalez. Multi-view fusion of sensor data for improved perception and prediction in autonomous driving. In *Proceedings of the IEEE/CVF Winter Conference on Applications of Computer Vision*, pages 2349–2357, 2022.
- [11] Wenyi Feng and Zhe Wang. Multi-view multi-manifold learning with local and global structure preservation. *Applied Intelligence*, 53(10):12908–12924, 2023.
- [12] Juan A Gallego, Matthew G Perich, Raaed H Chowdhury, Sara A Solla, and Lee E Miller. Long-term stability of cortical population dynamics underlying consistent behavior. *Nat. Neurosci.*, 23(2):260–270, February 2020.
- [13] Richard J Gardner, Erik Hermansen, Marius Pachitariu, Yoram Burak, Nils A Baas, Benjamin A Dunn, May-Britt Moser, and Edvard I Moser. Toroidal topology of population activity in grid cells. *Nature*, 602(7895):123–128, February 2022.
- [14] Victor Geadah, Gabriel Barello, Daniel Greenidge, Adam S Charles, and Jonathan W Pillow. Sparse-coding variational auto-encoders. *BioRxiv*, page 399246, 2018.
- [15] Scott Gigante, Adam S Charles, Smita Krishnaswamy, and Gal Mishne. Visualizing the phate of neural networks. *Advances in neural information processing systems*, 32, 2019.
- [16] Joshua Glaser, Matthew Whiteway, John P Cunningham, Liam Paninski, and Scott Linderman. Recurrent switching dynamical systems models for multiple interacting neural populations. *Adv. Neural Inf. Process. Syst.*, 33:14867–14878, 2020.
- [17] Evren Gokcen, Anna Jasper, Alison Xu, Adam Kohn, C Machens, and Byron M Yu. Uncovering motifs of concurrent signaling across multiple neuronal populations. *Adv. Neural Inf. Process. Syst.*, 2023.
- [18] Evren Gokcen, Anna I Jasper, João D Semedo, Amin Zandvakili, Adam Kohn, Christian K Machens, and Byron M Yu. Disentangling the flow of signals between populations of neurons. *Nat. Comput. Sci.*, 2(8):512–525, August 2022.
- [19] Ian Goodfellow, Jean Pouget-Abadie, Mehdi Mirza, Bing Xu, David Warde-Farley, Sherjil Ozair, Aaron Courville, and Yoshua Bengio. Generative adversarial nets. *Adv. Neural Inf. Process. Syst.*, 27, 2014.

- [20] Wolfgang Karl Härdle and Léopold Simar. Canonical correlation analysis. In *Applied Multivariate Statistical Analysis*, pages 431–442. Springer International Publishing, Cham, 2019.
- [21] Camille Jordan. Essai sur la géométrie à  $n$  dimensions. *Bulletin de la Société Mathématique de France*, 3:103–174, 1875.
- [22] James J Jun, Nicholas A Steinmetz, Joshua H Siegle, Daniel J Denman, Marius Bauza, Brian Barbarits, Albert K Lee, Costas A Anastassiou, Alexandru Andrei, Çağatay Aydın, Mladen Barbic, Timothy J Blanche, Vincent Bonin, João Couto, Barundeb Dutta, Sergey L Gratiy, Diego A Gutnisky, Michael Häusser, Bill Karsh, Peter Ledochowitsch, Carolina Mora Lopez, Catalin Mitelut, Silke Musa, Michael Okun, Marius Pachitariu, Jan Putzeys, P Dylan Rich, Cyrille Rossant, Wei-Lung Sun, Karel Svoboda, Matteo Carandini, Kenneth D Harris, Christof Koch, John O’Keefe, and Timothy D Harris. Fully integrated silicon probes for high-density recording of neural activity. *Nature*, 551(7679):232–236, November 2017.
- [23] Paris A Karakasis and Nicholas D Sidiropoulos. Revisiting deep generalized canonical correlation analysis. *arXiv [cs.LG]*, December 2023.
- [24] Stephen L Keeley, Mikio C Aoi, Yiyi Yu, Spencer L Smith, and Jonathan W Pillow. Identifying signal and noise structure in neural population activity with gaussian process factor models. *bioRxiv*, July 2020.
- [25] Hyunjik Kim and Andriy Mnih. Disentangling by factorising. In Jennifer Dy and Andreas Krause, editors, *Proceedings of the 35th International Conference on Machine Learning*, volume 80 of *Proceedings of Machine Learning Research*, pages 2649–2658. PMLR, 2018.
- [26] Dhruv Kohli, Alexander Cloninger, and Gal Mishne. Ldle: Low distortion local eigenmaps. *Journal of machine learning research*, 22(282):1–64, 2021.
- [27] Pei Ling Lai and Colin Fyfe. Kernel and nonlinear canonical correlation analysis. *International journal of neural systems*, 10(05):365–377, 2000.
- [28] Roy R Lederman and Ronen Talmon. Learning the geometry of common latent variables using alternating-diffusion. *Applied and Computational Harmonic Analysis*, 44(3):509–536, 2018.
- [29] Mihee Lee and Vladimir Pavlovic. Private-shared disentangled multimodal vae for learning of latent representations. In *Proceedings of the IEEE/CVF conference on computer vision and pattern recognition*, pages 1692–1700, 2021.
- [30] Kevin Z Lin and Nancy R Zhang. Quantifying common and distinct information in single-cell multimodal data with tilted canonical correlation analysis. *Proceedings of the National Academy of Sciences*, 120(32):e2303647120, 2023.
- [31] Qi Lyu, Xiao Fu, Weiran Wang, and Songtao Lu. Understanding latent correlation-based multi-view learning and self-supervision: An identifiability perspective. In *International Conference on Learning Representations*, 2021.
- [32] Michael F Mathieu, Junbo Jake Zhao, Junbo Zhao, Aditya Ramesh, Pablo Sprechmann, and Yann LeCun. Disentangling factors of variation in deep representation using adversarial training. *Advances in neural information processing systems*, 29, 2016.
- [33] Leland McInnes, John Healy, and James Melville. Umap: Uniform manifold approximation and projection for dimension reduction. *arXiv preprint arXiv:1802.03426*, 2018.
- [34] Kevin R Moon, David Van Dijk, Zheng Wang, Scott Gigante, Daniel B Burkhardt, William S Chen, Kristina Yim, Antonia van den Elzen, Matthew J Hirn, Ronald R Coifman, et al. Visualizing structure and transitions in high-dimensional biological data. *Nature biotechnology*, 37(12):1482–1492, 2019.
- [35] Noga Mudrik, Yenho Chen, Eva Yezerets, Christopher J Rozell, and Adam S Charles. Decomposed linear dynamical systems (dlDs) for learning the latent components of neural dynamics. *Journal of Machine Learning Research*, 25(59):1–44, 2024.
- [36] Theodoulos Rodosthenous, Vahid Shahrezaei, and Marina Evangelou. Multi-view data visualisation via manifold learning. *PeerJ Computer Science*, 10:e1993, 2024.
- [37] Sam T Roweis and Lawrence K Saul. Nonlinear dimensionality reduction by locally linear embedding. *science*, 290(5500):2323–2326, 2000.
- [38] Jürgen Schmidhuber. Learning factorial codes by predictability minimization. *Neural Comput.*, 4(6):863–879, November 1992.

- [39] João D Semedo, Amin Zandvakili, Christian K Machens, Byron M Yu, and Adam Kohn. Cortical areas interact through a communication subspace. *Neuron*, 102(1):249–259.e4, April 2019.
- [40] V Silva and J Tenenbaum. Global versus local methods in nonlinear dimensionality reduction. *Adv. Neural Inf. Process. Syst.*, pages 705–712, 2002.
- [41] Nicholas A Steinmetz, Cagatay Aydin, Anna Lebedeva, Michael Okun, Marius Pachitariu, Marius Bauza, Maxime Beau, Jai Bhagat, Claudia Böhm, Martijn Broux, Susu Chen, Jennifer Colonell, Richard J Gardner, Bill Karsh, Fabian Kloosterman, Dimitar Kostadinov, Carolina Mora-Lopez, John O’Callaghan, Junchol Park, Jan Putzeys, Britton Sauerbrei, Rik J J van Daal, Abraham Z Vollan, Shiwei Wang, Marleen Welkenhuysen, Zhiwen Ye, Joshua T Dudman, Barundeb Dutta, Adam W Hantman, Kenneth D Harris, Albert K Lee, Edvard I Moser, John O’Keefe, Alfonso Renart, Karel Svoboda, Michael Häusser, Sebastian Haesler, Matteo Carandini, and Timothy D Harris. Neuropixels 2.0: A miniaturized high-density probe for stable, long-term brain recordings. *Science*, 372(6539), April 2021.
- [42] Nils Sturma, Chandler Squires, Mathias Drton, and Caroline Uhler. Unpaired multi-domain causal representation learning. *Advances in Neural Information Processing Systems*, 36, 2024.
- [43] J B Tenenbaum, V de Silva, and J C Langford. A global geometric framework for nonlinear dimensionality reduction. *Science*, 290(5500):2319–2323, December 2000.
- [44] Joshua Tenenbaum and William Freeman. Separating style and content. *Adv. Neural Inf. Process. Syst.*, 9, 1996.
- [45] Joshua B. Tenenbaum, Vin de Silva, and John C. Langford. A global geometric framework for nonlinear dimensionality reduction. *Science*, 290(5500):2319–2323, 2000. Publisher: American Association for the Advancement of Science.
- [46] Laurens Van der Maaten and Geoffrey Hinton. Visualizing data using t-sne. *Journal of machine learning research*, 9(11), 2008.
- [47] Julius von Kügelgen, Yash Sharma, Luigi Gresele, Wieland Brendel, Bernhard Schölkopf, Michel Besserve, and Francesco Locatello. Self-supervised learning with data augmentations provably isolates content from style. *arXiv [stat.ML]*, June 2021.
- [48] Guoyin Wang, Chunyuan Li, Wenlin Wang, Yizhe Zhang, Dinghan Shen, Xinyuan Zhang, Ricardo Henao, and Lawrence Carin. Joint embedding of words and labels for text classification. In Iryna Gurevych and Yusuke Miyao, editors, *Proceedings of the 56th Annual Meeting of the Association for Computational Linguistics (Volume 1: Long Papers)*, pages 2321–2331, Melbourne, Australia, July 2018. Association for Computational Linguistics.
- [49] Weiran Wang, Raman Arora, Karen Livescu, and Jeff Bilmes. On deep multi-view representation learning. In *International conference on machine learning*, pages 1083–1092. PMLR, 2015.
- [50] Weiran Wang, Raman Arora, Karen Livescu, and Jeff Bilmes. On deep multi-view representation learning. In Francis Bach and David Blei, editors, *Proceedings of the 32nd International Conference on Machine Learning*, volume 37 of *Proceedings of Machine Learning Research*, pages 1083–1092, Lille, France, 2015. PMLR.
- [51] Weiran Wang, Raman Arora, Karen Livescu, and Jeff Bilmes. On deep multi-view representation learning: Objectives and optimization. *arXiv [cs.LG]*, February 2016.
- [52] Weiran Wang, Xinchun Yan, Honglak Lee, and Karen Livescu. Deep variational canonical correlation analysis. *arXiv preprint arXiv:1610.03454*, 2016.
- [53] Dingling Yao, Danru Xu, Sébastien Lachapelle, Sara Magliacane, Perouz Taslakian, Georg Martius, Julius von Kügelgen, and Francesco Locatello. Multi-view causal representation learning with partial observability. *arXiv preprint arXiv:2311.04056*, 2023.
- [54] Dingling Yao, Danru Xu, Sébastien Lachapelle, Sara Magliacane, Perouz Taslakian, Georg Martius, Julius von Kügelgen, and Francesco Locatello. Multi-view causal representation learning with partial observability. *arXiv [cs.LG]*, November 2023.
- [55] Yue Zhao, Xinge You, Shujian Yu, Chang Xu, Wei Yuan, Xiao-Yuan Jing, Taiping Zhang, and Dacheng Tao. Multi-view manifold learning with locality alignment. *Pattern Recognition*, 78:154–166, 2018.
- [56] Jun Zhuang, Lydia Ng, Derric Williams, Matthew Valley, Yang Li, Marina Garrett, and Jack Waters. An extended retinotopic map of mouse cortex. *Elife*, 6, January 2017.

## A Appendix / supplemental material

**LGN-V1 Training details** All encoders, decoders, and measurement networks consisted of 6 hidden layers of 200 units each. For geodesic distance calculation for all latent spaces, we averaged projections in a local neighborhood of 100 neighbors, and used 100 neighbors for the graph construction. We did not conduct a hyperparameter search, all hyperparameters described above were chosen based on intuition. All LGN-V1 models were trained on a GPU cluster using 5 RTX Quadro 5000 GPUs with 16GB of VRAM each (though the model uses much less). We did not use minibatches beyond what was required to distribute training across GPUs. To train the networks, we used the Adam optimizer with a learning rate of 0.001 that decayed linearly to  $1e-5$  over 25000 epochs. Results in the 4 show test set latents from a simulation that had 18,900 sample with a 80-20 train-test split.

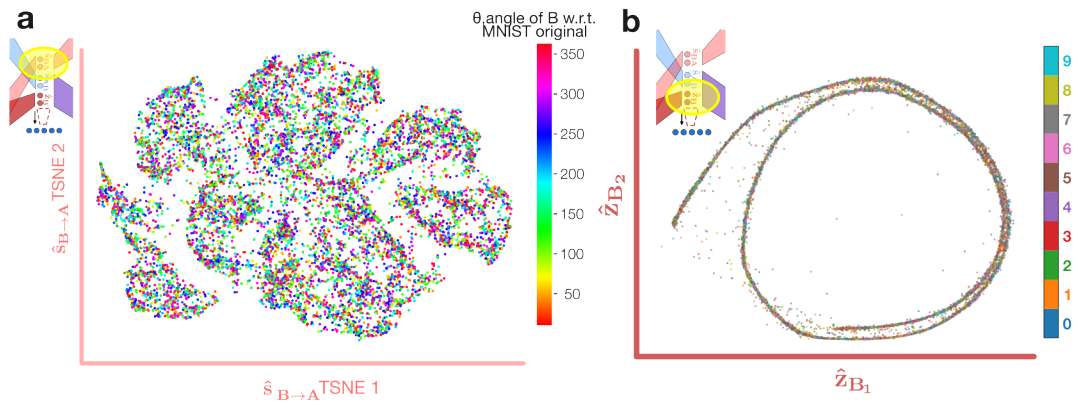
**MNIST Training details** Encoders, decoders, and measurement network architectures are described above. For geodesic distance calculation in all latent spaces, we averaged projections in a local neighborhood of 20 neighbors, and used 20 neighbors for the graph construction. We did not conduct a hyperparameter search, all hyperparameters described above were chosen based on intuition. The model was trained on the same GPU cluster as the LGN-V1 models. We used minibatches of size 20. To train the networks, we used the Adam optimizer with a learning rate of 0.001 that decayed linearly to  $1e-5$  over 20 epochs. 60,000 samples were used for training with 10,000 samples in the test set.

**MNIST Baseline details** To train the model from Lyu et al. we ran the provided code on our MNIST example using the same parameters as in [31]. Specifically, `lr_mmcca = 1`, `lr_min = 1e-3`, `mmcca_weight_decay = 1e-1`, `weight_decay = 1e-4`, `batch_size = 100`, `batch_size_mmcca = 1000`, `beta = 1`, and `_lambda = 100`. For the other baseline models, including DCCA, DCCAE, Karakasis et al., and DMVAE we selected optimal training parameters by running a grid searched over the following space of parameters: `lr: [1e-4, 1e-3, 1e-2, 1e-1]`, `weight_decay: [0, 1e-4, 1e-3, 1e-2, 1e-1]`, and `batch_size: [100, 200, 500, 800, 1000]`.

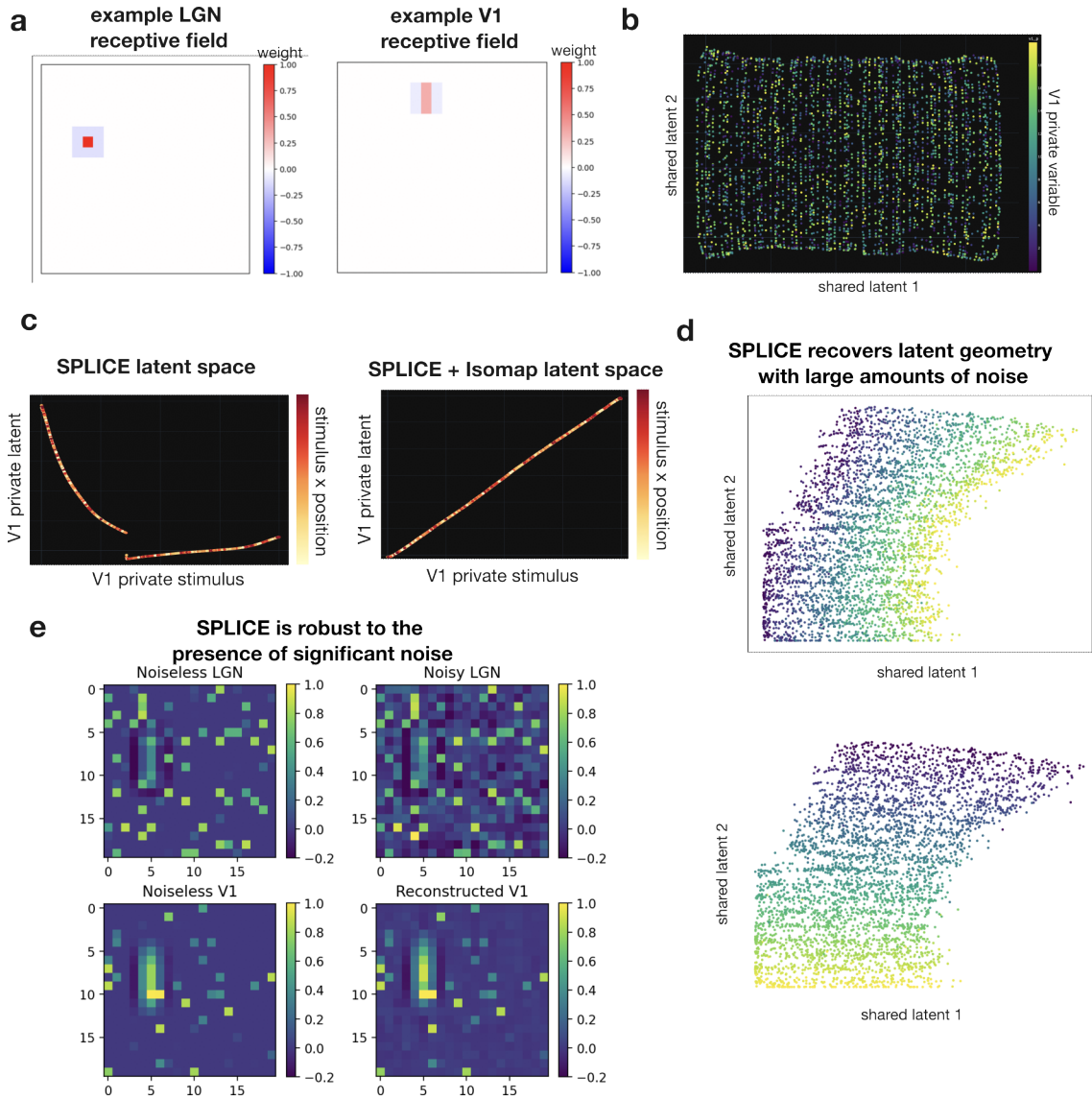
**Analysis of private angle subspaces.** To analyze the quality of the private subspaces and assess how well the private angle information was separated from the shared semantic information, we analyzed the variance of the estimated angle conditioned on a true, perturbed angle. Specifically, digits were rotated through 360 degree shifts at 1 degree intervals, and the variance of the estimated angle was calculated over 5 degree wide windows centered at 1 degree shift offsets. To correct for overall variability, we then divided the mean window variance by the overall private latent variance.

We noted that the estimated angle was at times offset by the inherent angle of the digits in the MNIST dataset; Some of the digits were written at an angle before any rotations were applied. To correct for the baseline angle, we identified for each digit a horizontal shift in the latent angle estimation by maximizing the inner product of each digit’s angle curve with a reference curve selected from one random digit. This offset was then subtracted to provide an absolute angle inclusive of the initial built-in angle.

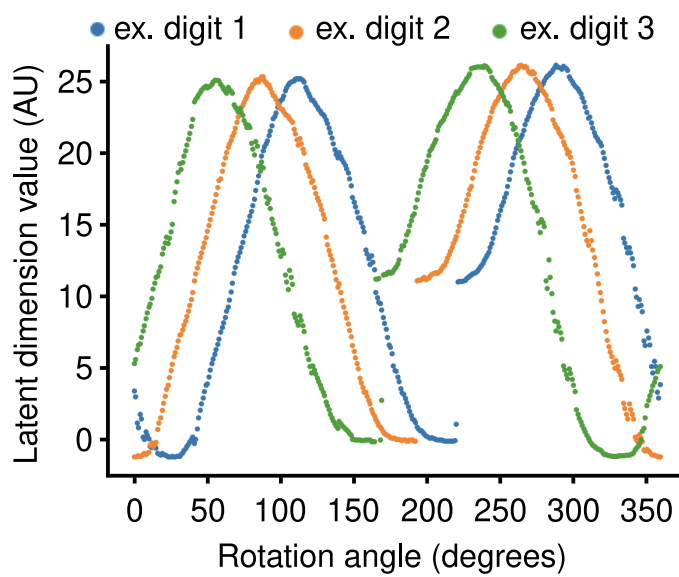
**Experiment 3 Training details** All encoders, decoders, and measurement networks consisted of 10 hidden layers of 100 units each. For geodesic distance calculation in all latent spaces, we did not average projections in a local neighborhood, and used 50 neighbors for the graph construction. All hyperparameters described above were chosen based on intuition. The model was trained on a single RTX 4080 GPU. To train the networks, we used the Adam optimizer with a learning rate of 0.001 that decayed linearly to  $1e-5$  over 5000 epochs. The dataset consisted of 13,872 timepoints, and we used a 80-20 train-test split that respected trial structure (all time points from the same trial belonged to the same split).



Supplementary Figure 1: **a)** MNIST SPLICE shared latent space from Fig. 2d colored by angle. **b)** MNIST SPLICE private latent space from Fig. 2b colored by digit class.



Supplementary Figure 2: **a)** Example receptive fields to shared stimulus for LGN and V1 simulated neurons. **b)** LGN-V1 SPLICE shared latent space from Fig. 4e, colored by V1 private stimulus. **c)** Private latent spaces corresponding to Fig. 4d and 4e, colored by shared stimulus x position. **d)** Inferred shared latent spaces for SPLICE fit to LGN-V1 simulation with IID Gaussian noise (Norm of noise =  $0.4 * \text{norm of noiseless simulation}$ ). Colored by stimulus x position (top) and stimulus y position (bottom) **e)** Example noiseless, input, and reconstructions for noisy simulation from **d)**



Supplementary Figure 3: Example curves of one private angular latent variables in the SPLICE model run on the rotated MNIST dataset. Three different digits (one in each color) show a tight oscillatory pattern over rotation angles, however each digit is offset from the others, indicating a different baseline angle at "0".